Marine Geology 379 (2016) 267–280

Contents lists available at ScienceDirect

Marine Geology

journal homepage: www.elsevier.com/locate/margo

Deep-water seamounts, a potential source of tsunami generated by landslides? The Hirondelle Seamount, NE Atlantic

Rachid Omira [a,b,*], Inês Ramalho [a], Pedro Terrinha [a,b], Maria Ana Baptista [b,c], Luis Batista [a,b], Nevio Zitellini [d]

[a] Instituto Português do Mar e da Atmosfera – IPMA, I.P., Rua C do Aeroporto, 1749-077 Lisbon, Portugal
[b] Instituto Dom Luiz – IDL, Faculdade de Ciências da Universidade de Lisboa, Campo Grande, Edifício C8, Piso 3, 1749-016 Lisbon, Portugal
[c] Instituto Superior de Engenharia de Lisboa – ISEL, Instituto Politécnico de Lisboa, Rua Conselheiro Emídio Navarro, 1, 1959-007 Lisbon, Portugal
[d] Istituto di Scienze Marine, CNR; 40129 Bologna, Italy

ARTICLE INFO

Article history:
Received 2 December 2015
Received in revised form 1 June 2016
Accepted 19 June 2016
Available online 20 June 2016

Keywords:
Submarine mass-failures
Deep-water seamount
Tsunamigenic potential
NE Atlantic

ABSTRACT

Submarine mass failures represent one of the most significant marine geo-hazards. Their importance as a major contributor to tsunami generation and hazard has been recognized over the last 20–30 years. This study investigates a newly mapped submarine landslide, the South Hirondelle Landslide (SHL), and its potential to generate a tsunami and to threat the surrounding coasts. The SHL is located 150 km offshore South West Iberia, along the southern flank of the Hirondelle Seamount. Here, available swath bathymetry and one multichannel seismic profile show the presence of large, geometrically well constrained, deep-water landslide deposit of about 500 km^3 and its associated scar. The failure likely occurred in one single event and according to a detailed numerical modelling of the landslide dynamics and of the resulting water propagation the mass failure generated a mega-tsunami, with significant impact along the surrounding coastal areas of Iberia and Morocco. This result strongly supports the inclusion of tsunami induced by deep-water submarine landslides in the marine geo-hazard assessment of the North East Atlantic region.

1. Introduction

Submarine mass-failures (SMFs) represent a widely recognized source of marine geo-hazards. They have the potential to generate significant morphological changes of the sea bottom and, in some cases, to damage large offshore infrastructures, particularly communication cables (Fine et al., 2005). Tsunamis generated by large SMFs are known to cause heavy coastal impact, particularly at local scales (Okal and Synolakis, 2004; Masson et al., 2006). Nevertheless, although their importance as contributors to tsunami hazard has been recognized over the last 20–30 years, they are seldom considered in the quantitative evaluation of tsunami hazard or in the design of tsunami warning strategies, mainly because they are hard to localize and monitor.

In spite of that, a number of large tsunamigenic SMFs events have been identified worldwide. The Storegga event is one of the largest prehistoric SMFs (7000 B.C.), with an estimated volume of 1700 km^3, that occurred on the continental slope west of Norway (Harbitz, 1992; Masson et al., 2006). According to both historical observations and numerical simulations (Harbitz, 1992; Bondevik et al., 2005), the Storegga slide triggered waves that flooded most of coastal areas around the Norwegian Sea and the North Sea. In 1929, the $M_w = 7.2$ Grand Banks earthquake caused the failure of ~200 km^3 of submarine sediments that travelled down slope for a distance of ~700 km from the source (Murty, 1977; Clague, 2001). The Grand Banks SMF caused a tsunami that killed at least twenty seven people in Newfoundland and one in Nova Scotia (Fine et al., 2005). A maximum run-up of 27 m was observed at Taylors Bay (Assier-Rzadkiewicz et al., 1997; Fine et al., 2005) and the waves were recorded as far as the Portuguese coasts and Azores islands (Fine et al., 2005). One of the widely studied SMF events has occurred in 1998, when a tsunami was generated following a $M_w = 6.9$–7.3 earthquake in Papua New Guinea. The first hypothesis associated the observed tsunami with the earthquake (Kawata et al., 1999; McSaveney et al., 2000). However, later studies revealed that the fault dislocation was unable to produce a wave fitting the arrival time and tsunami heights distribution observed in the near-field (Heinrich et al., 2000; Tappin et al., 2001; Imamura et al., 2001). A SMF source was then proposed and evidence was found to support this hypothesis (Heinrich et al., 2000; Imamura et al., 2001; Synolakis et al., 2002). Tappin et al. (2001) simulated the Papua New Guinea tsunami from an underwater landslide, 750 m thick, involving an approximate volume of 7 km^3 of cohesive sediments, obtaining run-up and wave heights in good agreement with the observed ones.

SMFs are almost impossible to observe and characterize, therefore, numerical modelling remains one of the key ways to understand the SMFs dynamics and to assess the associated tsunami (Harbitz et al., 2006). According to Masson et al. (2006) various mechanisms can

* Corresponding author at: Instituto Português do Mar e da Atmosfera – IPMA, I.P., Rua C do Aeroporto, 1749-077 Lisbon, Portugal.
E-mail address: omirarachid10@yahoo.fr (R. Omira).

http://dx.doi.org/10.1016/j.margeo.2016.06.010
0025-3227/

trigger submarine landslides, including: i) earthquakes, ii) sea-level rise, iii) overpressure due to rapid deposition, vi) presence of weak sediment layers, and v) oversteepened slopes.

In the NE Atlantic, less emphasis has been given so far to tsunamigenic landslide compared to the tsunamis of seismic origin, despite SMFs may occur more frequently than expected. In fact, Lo Iacono et al. (2012) have recently shown the evidences of large SMFs in the Gorringe Bank, with significant tsunami potential and impact along the surrounding coasts of the NE Atlantic region.

In this paper, we study a large SMF found in the NE Atlantic and its possible tsunamigenic potential. The study is based on an available multichannel seismic profile and multi-beam swath bathymetric data which allowed to define the geomorphologic characteristics of the landslide including the evacuation and depositional areas. The identified SMF is located in the south flank of Hirondelle Seamount, NE Atlantic, 100 km west of the Gorringe Bank (see Fig. 1 for localization). The investigation of the South Hirondelle Landslide (SHL) includes: i) localization and measure of the landslide source area and deposit, ii) landslide failure scenarios: one single event versus multiple events, and iii) modelling of the tsunami generation potential and propagation towards the target coasts. We further discuss the SHL age and its possible trigger mechanism as well as the numerical modelling limitations.

2. The Hirondelle Seamount: geological setting and landslide

2.1. Geological setting

The Hirondelle Seamount is located along the Eurasia-Africa plate boundary in the Atlantic Ocean. This plate boundary is well defined only between the Azores plateau and the Madeira-Tore Rise (MTR in Fig. 1), where the boundary is discrete and accommodated by a dextral strike-slip fracture zone, the Gloria Fault (GF in Fig. 1), along which instrumental earthquakes of $M_w = 7.1–8.4$ (Bird and Kagan, 2004; Buforn et al., 1988) were recorded (Fig. 1).

To the east of the MTR, the location of the plate boundary is still a subject of debates and research. The role of plate boundary has been assigned to two lithospheric tectonic structures, the subduction zone underneath the Gibraltar Arc (Gutscher et al., 2002) and the South-West Iberia Margin (SWIM in Fig. 2) dextral strike-slip faults between Europe and Africa (Zitellini et al., 2009) (Fig. 1). Besides these two lithospheric fault zones a series of thrust faults with demonstrated activity in the Quaternary have been studied by several authors and summarized in Zitellini et al. (2004) (Fig. 2). The main landslides described in southwest Iberia are associated with these thrust faults: the Marquês de Pombal (260 km^2) landslide and Gorringe landslide (380 km^2), both showing active deformation, frontal thrust fault scarps of 1.4 km and 5 km height, respectively, and clusters of seismicity (Gràcia et al., 2003; Terrinha et al., 2003; Lo Iacono et al., 2012) (Figs. 1 and 2).

The Hirondelle Seamount (Hsm) is located east of the MTR, between the Josephine Seamount (Jsm) and the Gorringe Bank (GB) (Fig. 1). The alignment of these three seamounts forms an ESE-WNW oriented continuous ridge about 300 km long and about 80 km wide, which separates the Horseshoe Abyssal Plain (HAP in Fig. 2) from the Tagus Abyssal Plain (TAP in Fig. 2) and where most of the seismicity associated to the Europe-Africa plate boundary is located. The Hsm is made up of oceanic crust of Upper Jurassic age, chron M21 after Seton et al. (2012). Southward of the Hirondelle-Gorringe seamounts are located the Coral Patch Seamount (CPsm in Fig. 2) and the Coral Patch Ridge. These seamounts separate the Seine Abyssal Plain from the Horseshoe Abyssal Plain and were affected by thrusting and folding during the Miocene (Zitellini et al., 2004). Despite recent deformation has been described based on seismic reflection data, the recorded seismicity associated is low (Martinez-Loriente et al., 2013, Fig. 2).

Although the published information on the Josephine and Hirondelle seamounts is scarce, the Gorringe Bank has been widely investigated with seismic reflection and refraction, swath bathymetry (Sartori et al., 1994; De Alteriis et al., 2003), manned dives (Girardeau et al., 1998) and by an Ocean Drilling Project drill (Ryan et al., 1973). The Gorringe Bank is a piece of exhumed lithospheric mantle carried on

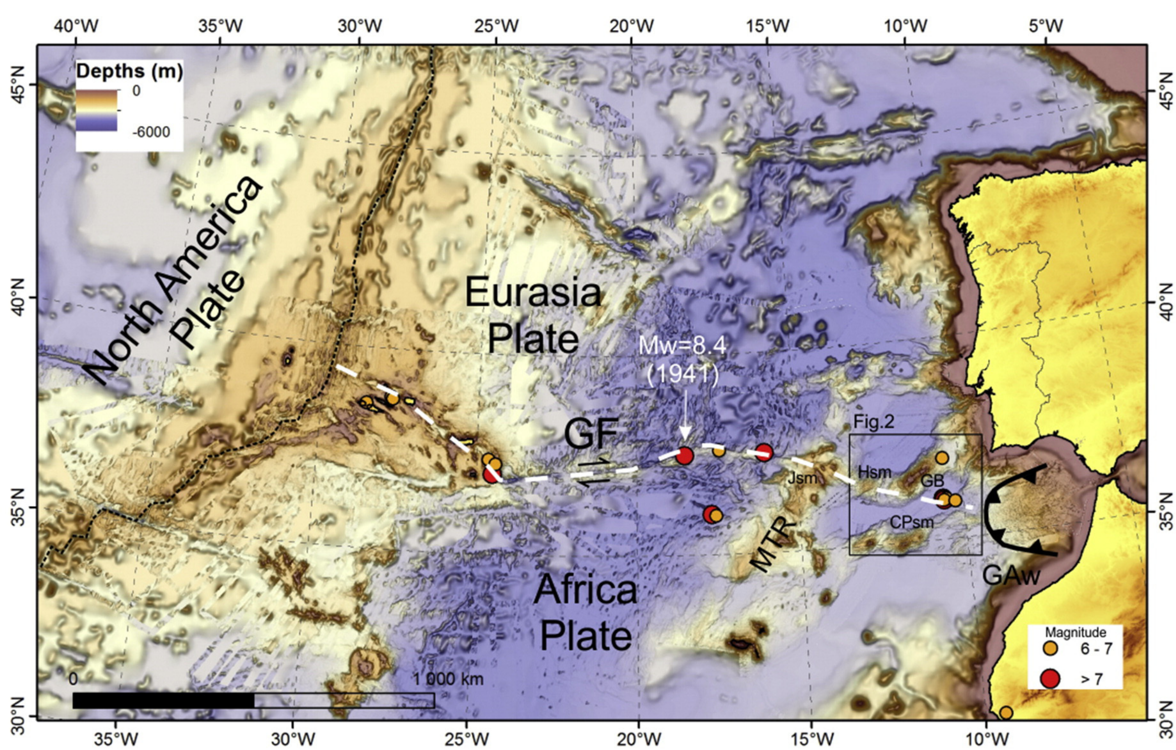

Fig. 1. Location of the study area with bathymetry of a part of the North Atlantic encompassing the study area (black square). Red and yellow circles mark the epicenters of instrumental earthquakes M > 6. MTR, Madeira-Tore Rise; GF, Gloria Fault; GAw, Gibraltar Accretionary wedge; Jsm, Josephine Seamount; Hsm, Hirondelle Seamount. (For interpretation of the references to colour in this figure legend, the reader is referred to the web version of this article.)

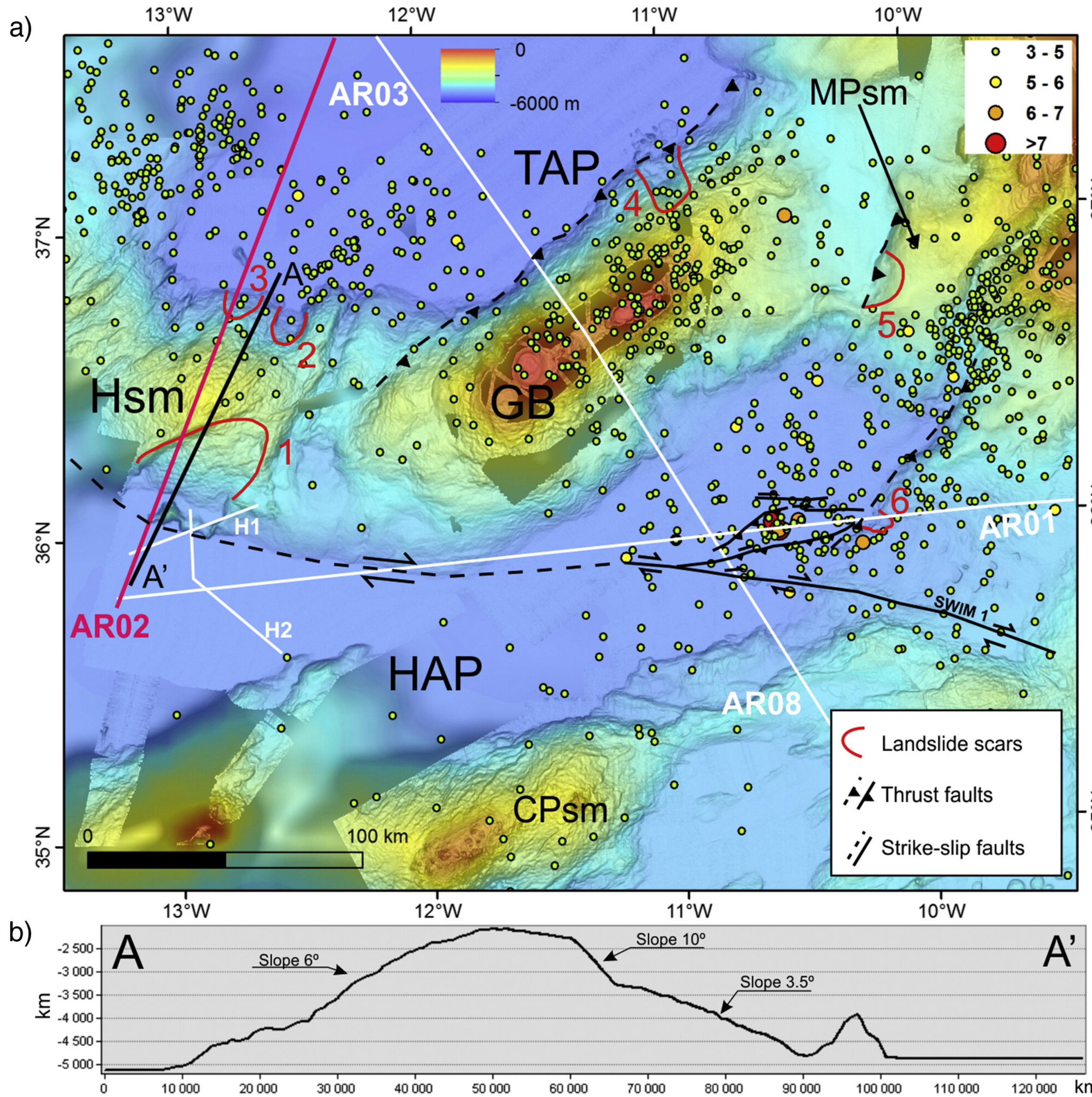

Fig. 2. Morphology and tectonics of the study area: a) Bathymetry of the Hirondelle seamount and neighbour area and main tectonic features: fault interference pattern between Horseshoe thrust and SWIM strike-slip faults. Location of landslides: 1) South Hirondelle Landslide (SHL) (this study); 2 and 3) North Hirondelle; 4) North Gorringe (Lo Iacono et al., 2012); 5) Marquês de Pombal (Gràcia et al., 2003; Terrinha et al., 2003) and 6) Horseshoe (in prep.). Seismic reflection also shown: AR02 is shown in Fig. 3; AR01 (Torelli et al., 1997), AR03 and AR08 (Sartori et al., 1994); H1 and H2 (Hayward et al., 1999). GB, Gorringe Bank; HAP, Horseshoe Abyssal Plain; Hsm, Hirondelle seamount; MPsm, Marquês de Pombal seamount; TAP, Tagus Abyssal Plain; CPsm, Coral Patch seamount; b) Bathymetric profile across the Hirondelle Seamount and South Hirondelle Landslide.

top of a north-westward directed thrust for approximately 20 km mostly during Miocene times (Hayward et al., 1999; Sartori et al., 1994; Auzende et al., 1978; Jiménez-Munt et al., 2010; Sallarès et al., 2013). The recent tectonic activity of the Josephine-Gorringe ridge is attested by instrumental seismicity whose focal mechanisms indicate a maximum horizontal stress parallel to NW-SE direction (Geissler et al., 2010).

There are various chrono-stratigraphic models used for calibrating the seismic reflection data of the HAP, all based on the DSDP sites 135 and 120 drillings on the Coral Patch Ridge and Gorringe Bank by Hayes et al. (1972) and Ryan et al. (1973) respectively, and on the ODP 339 in the Gulf of Cadiz (Hernández-Molina et al., 2014). Hayward et al. (1999) showed a MCS profile south of the Hsm producing the first stratigraphic model of the study area that consists of six seismic units on top of acoustic basement. Table 1 shows the correspondence between seismic units identified in this work and those of Hayward et al. (1999). For identifying the base of Quaternary we used the model by Roque (2007) and Roque et al. (2012). The existence of Holocene hemipelagic deposits on the seafloor of the HAP and at the foot of the Marquês de Pombal thrust was confirmed by Gràcia et al. (2010). For estimating the thickness of the slide we used the depth conversion velocities by Martinez-Loriente et al. (2013).

2.2. The Hirondelle Seamount and the South Hirondelle Landslide

The Hirondelle Seamount is a west to east trending seamount rising >2800 m above the HAP and 3000 m above the TAP. An ENE-WSW striking scarp dipping 14° SE separates an area to the northwest where a

Table 1
Correlation between stratigraphic models in the West Horseshoe Abyssal Plain.

This work	Hayward et al. (1999)
UIV- Holocene – Lower Miocene	WHI- Pleistocene-Late Oligocene
UIII- Oligocene – Early Aptian	WHII–WHIII-Early Eocene to early Aptian
UII- Early Aptian to Late Jurassic	WHIV–WHV-Early Aptian to Late Jurassic
UI- Early Aptian to Late Jurassic	WHVI- Early Aptian to Late Jurassic
Acoustic Basement- Jurassic oceanic crust	Acoustic Basement- Upper Jurassic

pervasive NE-SW trending linear fabric occurs from an area to the southeast where this fabric is absent and the seafloor morphology is smoother and wrinkled, corresponding to the South Hirondelle Landslide (SHL) (1 in Fig. 2). The structure of the Hsm, the seismic stratigraphic model and the internal geometry of the SHL are described based on the interpretation of the multichannel seismic reflection profile AR02 (Fig. 3) that cuts across the Hsm although not parallel to the main dip direction of the SHL.

This seismic profile was acquired in 1992 by the R/V OGS Explora using an array of 32 guns for a total volume of 5000 in.^{3} and a 120-channel streamer with group interval of 25 m and shot interval of 50 m. The record length was 13 s with 2×10^{-3} s sample interval. The processing was

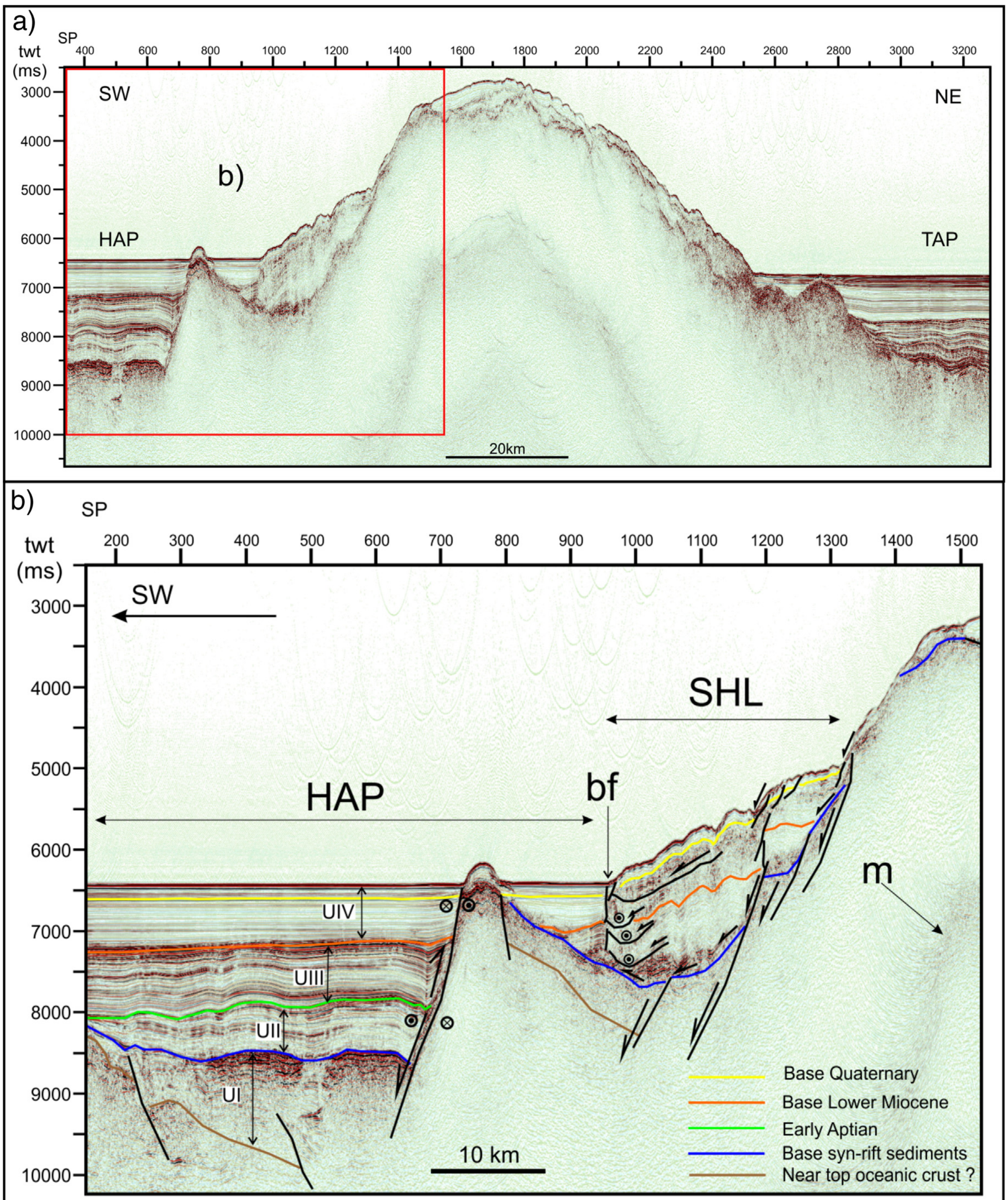

Fig. 3. Seismic reflection line AR02: a) Uninterpreted full line across the Hirondelle seamount; b) Interpretation of the southern part of AR02 across the South Hirondelle Landslide.

carried out at the Institute of Marine Science (ISMAR) of Bologna using the DISCO package of COGNISEIS Development Inc. applying a standard processing sequence. The seismic processing sequence can be summarized as follows: demultiplexing, resampling to 4×10^{-3} s, sorting, spike deconvolution, velocity analysis every 2.5 km, normal move out, muting, CDP staking, spherical divergence correction, finite-difference wave-equation migration, time-variable filtering.

The seismic reflection line AR02 images the stratigraphic record and tectonic structure across the Hsm (Fig. 3a) and part of the HAP and TAP. On the southern flank of the seamount, the internal structure of the SHL, a rotational slide, is depicted (Fig. 3b). The basal failure has a concave curvature over the whole length implying reduced down-slope displacement. Extensional deformation is accommodated down dip in the head of the landslide, as faults cutting through the whole body of the landslide or affecting its topmost layer only (Fig. 3b). Shortening is accommodated in the toe thrust part (up dip) and central part of the slide. The existence of a buttress fault (bf) against which shortening builds up may indicate that this acted as a lateral ramp to the main slide movement. Actually, the MCS AR02 profile is not parallel to the main slope dip parallel to which the slide movement could have occurred.

The maximum thickness of the deformed slide is approximately 1.6 s TWT, calculated as follows. Using the velocity model in Martinez-Loriente et al. (2013) for the equivalent layers in MCS AR02 we can assign a layer velocity of 2000 $m \cdot s^{-1}$ to UIV and a mean velocity of 2800 $m \cdot s^{-1}$ for the underlying layers. The maximum thickness of UIV (0.7 s TWT) corresponds to 700 m and the underlying package (0.9 s TWT) corresponds to 1260 m, a total thickness of 1960 m, roughly.

In the Horseshoe Abyssal Plain we identified four main seismo-stratigraphic units, UI to UIV above the acoustic basement (Fig. 3b). UI is the lowest seismic unit that displays organized stratified reflections. It lays on top of acoustic basement that should correspond to oceanic crust of Late Jurassic age, according to general agreement (Seton et al., 2012; Sallarès et al., 2013; Martinez-Loriente et al., 2013). The wedge shape of UI and UII indicates that these units were deposited during tectonic extension, i.e., intra-oceanic rifting. The lateral discontinuity of reflectors within horizons in UI suggests tectonic structuring of this block and the presence of sediments of variable composition, compatible with the presence of volcano-clastics. Above UI, reflectors are more continuous indicating that tectonic extension concentrated on the main fault during the deposition of UII. UIII also shows slightly undulated – parallel and laterally continuous reflections suggesting the presence mostly of hemipelagic sediments; the constant thickness indicates this is a post-extension sequence. Coherent folding of UI–UII–UIII indicates that tectonic shortening occurred previous to deposition of UIV, which lies on top of folded UIII displaying parallel, laterally continuous reflections. UIV is clearly a post tectonic shortening unit showing minor drag at the contact with the rotated basement block shown in Fig. 3b. We interpret the faults that appear in the uppermost part of the SHL (Fig. 3b) as gravity faults and disruptures caused by the landslide movement. While in the southernmost part of the AR02 line (Fig. 3b), the fault is deep seated and has a long lived history of rifting and inversion, previous to the deposition of UIV. Inspection of available and published seismic reflection lines in the study area (see Fig. 2a for location) shows that the top of the folded horizons of UIII are covered by sediments that are lateral equivalent of the Allochthonous unit of the Gulf of Cadiz (Medialdea et al., 2004). Accordingly, the base of the UIV is considered to be of Early Miocene age, also in agreement with Fig. 3 of Torelli et al. (1997).

Stratigraphic correlation of the seismic units of the HAP and top of the Hsm is not possible because the lack of lateral continuity of the reflectors across the landslide headscarp. However, it is straightforward that the crest of the seamount is covered by a package of condensed stratigraphic series, indicating that the Hsm was a structural high at the time of formation of the Lower Jurassic oceanic crust.

The stratigraphic correlation between the HAP and SHL was attempted and is shown in Fig. 3. Two seismic horizons (base Quaternary and UIV–UIII boundary) were correlated from the HAP across the acoustic basement peak at shot point 750. Sub-division of UIII to UI within the SHL was not possible due to the homogenization of the seismic character caused the deformation of the slid body. Nevertheless, comparison of the acoustic character at the base of the landslide suggests that the main decollement surface to the SHL is near the UI–UII boundary (Fig. 3b).

The joint interpretation of the AR02 seismic reflection profile (Fig. 3b) and swath bathymetry (Fig. 4a) allows the characterization of the SHL, as follows: i) The wrinkled surface of the slope corresponds to folded strata of a slid body; ii) The larger wave-length folds affect the UII through UIV sedimentary sequence; iii) Minor folds are observed at the top of the youngest sedimentary horizons, as well as interbedded in deeper packages, indicating existence of internal detachments that account for localized non-harmonic folding of the whole body; the detailed inspection of non-harmonic folding and internal bed cut offs allowed for interpretation of detachment faults in the slid body; iv) internal shortening of the slide terminates against a vertical buttress fault (bf in Fig. 3b); the presence of a channel shaped extensional detachment horizon suggests that the main slide direction is not parallel to the profile section, but rather probably towards the southeast, i.e., parallel to the main slope dip.

The main morphologic features of the SHL were identified in the swath bathymetry model depicted in Fig. 4a. The SHL covers a total

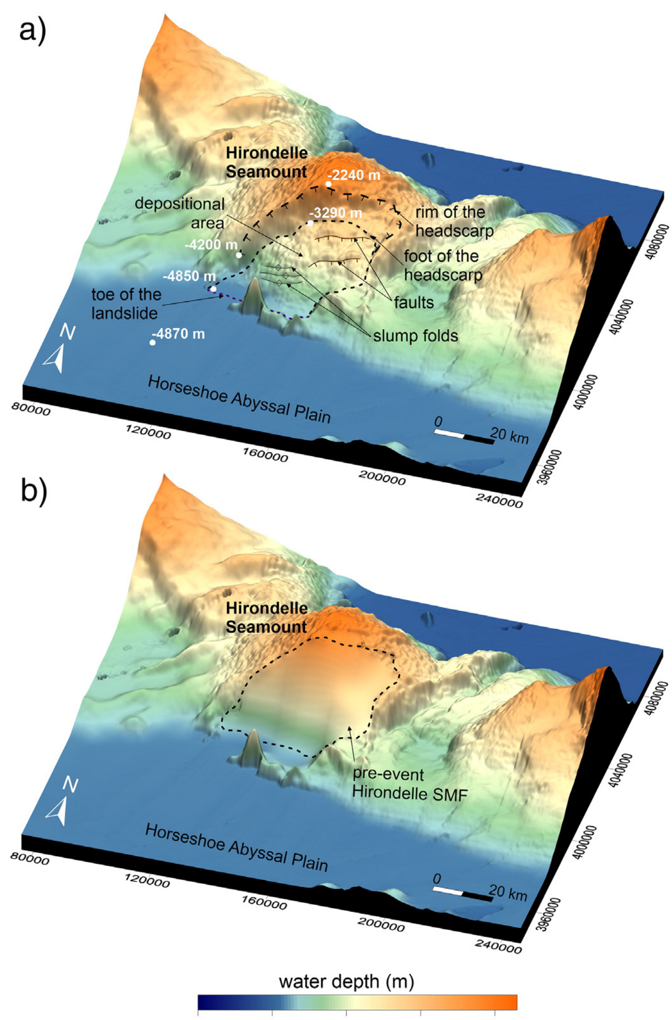

Fig. 4. Bathymetric models: a) Post-event (present day) bathymetric model including the main morphologic features of the South Hirondelle Landslide; b) Pre-event, including the reconstruction of the South Hirondelle Landslide, bathymetric model. The maps coordinates system is UTM – Zone 29 N, Datum WGS-84.

area of ~1200 km^2 comprising erosion and depositional areas. The SHL source area extends for ~80-km-long with slopes varying from ~3.5° to ~16°. The rim of the headscarp, standing in the upper limit of the source area, has a curvilinear shape with two main orientations (Fig. 4a). The western part coincides with the WSW-ENE striking oceanic rift faults, suggesting that it is controlled by an inherited tectonic fabric. The northern part of the headscarp is parallel to the Hsm crest, normal to the dip of the seamount, suggesting that this segment of the scarp has a gravity control only. The rim of the headscarp is located at depths −2240 m to −4200 m with a maximum slope of 16° SSE. The depositional area covers ~680 km^2. It is bounded at the top by the foot of the headscarp, located at −3290 m depth, and at the bottom by the foot of the landslide, located at −4850 m depth (Fig. 4a). Slopes within this area vary from ~0.2° up to ~3.5°. Comparison of the swath bathymetry (Fig. 4a) with the MCS profile (Fig. 3b) allowed the interpretation of additional SHL morphologic features, such as internal faults and slump folds as marked in Fig. 4a. At the base of the SHL the bathymetry model allowed outlining the lateral extent of the buttress fault/toe of the landslide identified in the seismic profile.

3. Tsunamigenic potential and wave propagation

3.1. Methodology and data

To assess the tsunami generation potential and wave impact posed by the failure of the SHL, we employ a numerical modelling methodology that considers a realistic pre-event bathymetry model, that uses a sensitivity analysis to constrain the material parameters of the landslide from the observed deposit, and that uses a "two-way" coupling model, taking into account the effect of the slide on the water and the effect of the wave on the slide. This later effect is more important in the case of shallow-water landslides where the generated wave can affect the landslide motion (Jiang and LeBlond, 1994). Our methodology consists of five steps that include: i) build the pre-mass failure bathymetric model, ii) run multiple times the landslide flow simulations with varied landslide body physical parameters (i.e., density, kinematic viscosity, and drag coefficient), iii) compare the simulated landslide run-out mass with the landslide deposit identified in the bathymetry and multichannel seismic profiles, iv) select the landslide physical parameters for which the simulations lead to a better representation of the observed deposit, v) run, using the selected physical parameters, the "two-way" coupling model that simulate the landslide-induced tsunami generation and propagation.

3.1.1. Pre-event bathymetric model

In order to model properly the mass-failure motion it is necessary to infer the pre-event bathymetric model, taking into account the landslide deposit and the source area. The pre-failure sea-bottom topography can be inferred by restoring in the original position the sedimentary package involved in the slide using the swath bathymetry and the multichannel seismic profile AR02. From the AR02 line we can infer the amount of shortening suffered by the individual units U1–UVI by unfolding strata showing consistent lateral continuity. This exercise will allow determining the rough amount of the horizontal mass movement and the original thickness of the landslide deposit. Once these numbers are known we can restore the position and arrangement of the sediments taking into account the conservation of the SMF volume.

Fig. 4 depicts both post-event (Fig. 4a) and the pre-event (Fig. 4b) bathymetric models. Analysis of the post-event bathymetric model results in a volume of about 500 km^3 of depositional material. In Fig. 4b we build the pre-event SHL with respect to the depositional volume and the origin area of the failure. The SMF material is distributed in order to cover the origin area of the landslide body and conserve the landslide depositional volume. In Fig. 5a, we plot profiles of the observed deposit (MCS profile AR02, in Fig. 3a) and the reconstructed SHL.

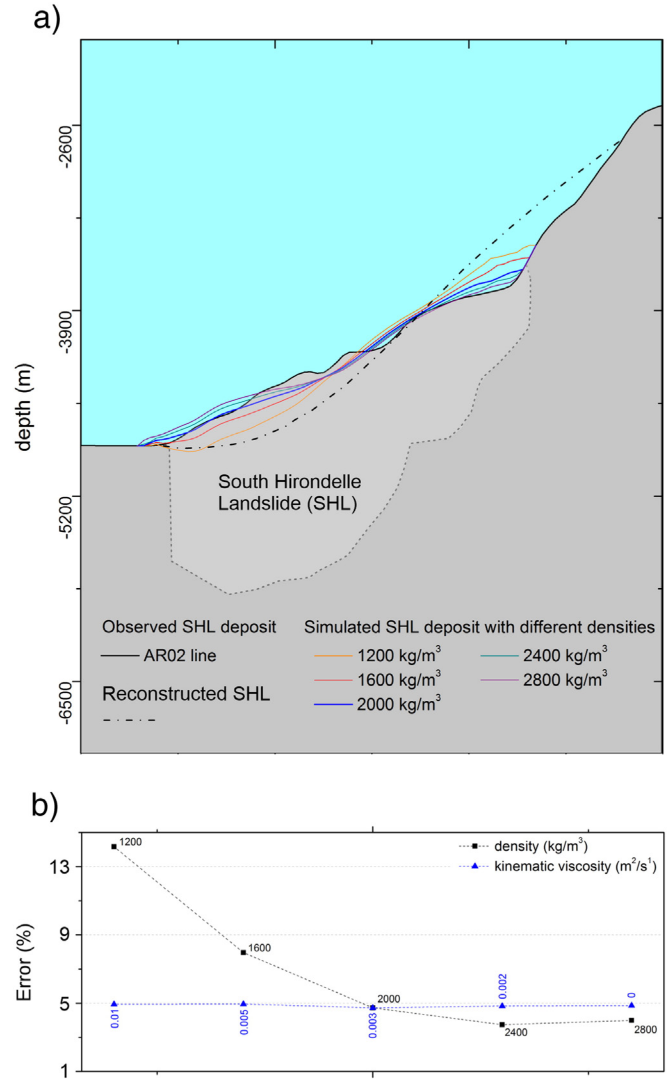

Fig. 5. Sensitivity analysis of the South Hirondelle Landslide movement to the physical material parameters: a) comparison between the observed (black profile) and the simulated deposits considering different landslide densities. Dashed black profile corresponds to the reconstructed pre-event SHL. All profiles are extracted at the same location as the MCS profile AR02 depicted in Fig. 3a; b) error associated to the misfit between the observation and the simulations: the black dashed curve indicates the error associated to the influence of the density parameter on the SHL behaviour considering fixed drag coefficient ($C_d = 0.0030$) and kinematic viscosity ($\nu = 0.01\ m^2 \cdot s^{-1}$); the blue dashed curve indicates the error associated to the influence of the drag coefficient for fixed density ($\rho_2 = 2000\ kg \cdot m^{-3}$) and kinematic viscosity ($\nu = 0.01\ m^2 \cdot s^{-1}$). (For interpretation of the references to colour in this figure legend, the reader is referred to the web version of this article.)

3.1.2. Numerical modelling

To simulate both the movement of the landslide body and the wave generated by the seafloor deformation we employ a multi-layers viscous shallow-water (VSW) model (Jiang and LeBlond, 1994). The lower layer represents the landslide that is assumed to be a viscous-incompressible fluid, and characterized by sediment density, kinematic viscosity and horizontal velocity. The landslide is bounded by the upper layer consisting of seawater assumed to be inviscid and incompressible. The motion of the underwater landslide body and the generation and propagation of the subsequent tsunami are governed by Eqs. (1.1), (1.2), and (1.3) and (2.1), (2.2), and (2.3), respectively. Eqs. (1.1), (1.2), and (1.3) and Eqs. (2.1), (2.2), and (2.3), presented in Cartesian coordinates, constitute an adapted version of the VSW model of Jiang and LeBlond (1994) that includes a realistic bottom bathymetry (Thomson et al., 2001; Fine et al., 2003; Rabinovich et al., 2003). Also, to account for the drag effects we integrate a quadratic function in the last terms of the momentum conservation equations of the landslide (Fine et al., 2005).

$$\frac{\partial D}{\partial t}+\frac{2}{3}\left[\frac{\partial (DU)}{\partial x}+\frac{\partial (DV)}{\partial y}\right]=0 \tag{1.1}$$

$$\begin{aligned}&\frac{3}{2}\frac{\partial U}{\partial t}-\frac{2}{15}\frac{U}{D}\frac{\partial D}{\partial t}+\frac{8}{15}\left[\left(U\frac{\partial U}{\partial x}+V\frac{\partial U}{\partial y}\right)\right]\\&\quad=-\frac{g}{\rho_2}\left[(\rho_2-\rho_1)\left(\frac{\partial D}{\partial x}-\frac{\partial h_s}{\partial x}\right)+\rho_1\frac{\partial \eta}{\partial x}\right]-\frac{2\nu U}{D^2}+C_d\frac{U|U|}{D}\end{aligned} \tag{1.2}$$

$$\begin{aligned}&\frac{3}{2}\frac{\partial V}{\partial t}-\frac{2}{15}\frac{V}{D}\frac{\partial D}{\partial t}+\frac{8}{15}\left[\left(U\frac{\partial V}{\partial x}+V\frac{\partial V}{\partial y}\right)\right]\\&\quad=-\frac{g}{\rho_2}\left[(\rho_2-\rho_1)\left(\frac{\partial D}{\partial y}-\frac{\partial h_s}{\partial y}\right)+\rho_1\frac{\partial \eta}{\partial y}\right]-\frac{2\nu V}{D^2}+C_d\frac{V|V|}{D}\end{aligned} \tag{1.3}$$

$$\frac{\partial (h_s+\eta-D)}{\partial t}+\frac{\partial (h_s+\eta-D)}{\partial x}+\frac{\partial (h_s+\eta-D)}{\partial y}=0 \tag{2.1}$$

$$\frac{\partial u}{\partial t}+u\frac{\partial u}{\partial x}+v\frac{\partial u}{\partial y}=-g\frac{\partial \eta}{\partial x} \tag{2.2}$$

$$\frac{\partial v}{\partial t}+u\frac{\partial v}{\partial x}+v\frac{\partial v}{\partial y}=-g\frac{\partial \eta}{\partial y} \tag{2.3}$$

where D is the thickness of the landslide; η is the ocean free surface displacement; ν is the kinematic viscosity, h_s is the static water depth; u,v,U,V are the horizontal components of the velocities in x- and y-direction of the wave and landslide, respectively; g is the gravity acceleration; C_d is the drag coefficient; and $\rho_1$and ρ_2 are the densities of the water and the landslide, respectively.

The governing equations (Eqs. (1.1), (1.2), and (1.3) and (2.1), (2.2), and (2.3)) were solved in an explicit leap-frog finite-difference scheme, with an upwind method for the advection terms. To ensure the numerical stability of the simulations a Courant-Friedrich-Levy condition as well as artificial viscosities for the landslide and the wave were considered.

We consider the pre-event bathymetric model (Fig. 4b) and we run the landslide motion code (governed by Eqs. (1.1), (1.2), and (1.3)) for different landslide "scenarios". Each scenario is characterized by specific physical material parameters (density, kinematic viscosity, and drag coefficient). Then we compare the simulated deposit with the landslide run-out mass until getting the SMF "scenario" that better fits the observed deposit. Both the density and the drag coefficient were subjected to a sensitivity analysis to evaluate their influence on the SHL movement. Fig. 5a shows a comparison between the observed (MCS profile AR02, in Fig. 3a) and the simulated deposits considering different landslide densities. The error associated to the misfit between the observation and the simulations considering different density values and drag coefficients is calculated and the results are depicted in Fig. 5b. Using these results, we selected the parameters that lead to the smaller error (~5%, see Fig. 5b), excluding the high density values ($\rho_2 > 2000\ \mathrm{kg\cdot m^{-3}}$) assumed to be inappropriate for our case study (Hayes et al., 1972; Schmincke et al., 1995). On the other hand, the numerical tests carried out considering different kinematic viscosity values ($\nu < 1\ \mathrm{m^2\cdot s^{-1}}$) show that there is no noticeable influence of this parameter on the SHL motion due to the large volume involved, which led us to adopt a viscosity value from the published literature on the SMFs (Fine et al., 2003; Rabinovich et al., 2003; Fine et al., 2005). Therefore, to assure a good representation of the deposited material, we assumed a landslide density of $2000\ \mathrm{kg\cdot m^{-3}}$ with a kinematic viscosity of $0.01\ \mathrm{m^2\cdot s^{-1}}$, and a drag coefficient of 0.0030. Finally, for this scenario we ran the "two-way" coupling model (Eqs. (1.1), (1.2), (1.3), (2.1), (2.2), and (2.3)) for tsunami generation and propagation.

The tsunami potential and impact posed by the occurrence of the Hirondelle SMF is assessed through modelling of the tsunami generation, propagation and coastal impact considering the SMF scenario that well reproduces the observed deposit.

3.2. Assessment of tsunami potential and coastal hazard

3.2.1. Potential of tsunami generation

The landslide-induced tsunami generation results from the deformation of the sea-bottom caused by the motion of the SHL body. Fig. 6 depicts the potential of tsunami generation following the motion of the SHL body along the slope. We plot the time evolution of both the lower layer representing the SHL thickness during its motion and the upper layer of the subsequent sea free-surface perturbation. The snapshots are presented from the initiation of the failure ($t = 0$ s) until that the SMF body stops sliding and regains its equilibrium ($t = 120$ s).

Unlike the almost instantaneous generation of earthquake-tsunamis, the SMF-induced tsunami generation is a time-dependent evolutionary process. In the case of the Hirondelle SMF, after ~60 s from the initiation of the motion of the landslide body (Fig. 6b) a significant perturbation of the sea surface is caused. The wave amplitude reaches about 40 m at this stage of the SMF motion. Due to the large volume involved and the fact that the sediments do not run-out far from the source area, the numerical simulations shows that the SHL reaches the equilibrium after ~2 min of motion (see Fig. 6c). At this stage the tsunami generation is completed and the wave reaches 38 m in amplitude.

The computed sea-surface perturbation shows that a mega-tsunami is generated following the failure of a sediments volume of about 500 $\mathrm{km^3}$ at the Hsm. This tsunami can cause significant impact when propagating towards the surrounding coastal stretches that are relatively close to the SMF source zone.

In Fig. 7 we plot the modelled velocity field of the SHL during its motion down slope. The velocity snapshots are presented at $t = 30$ s (Fig. 7a), at $t = 60$ s (Fig. 7b), and at $t = 90$ s (Fig. 7c) after the landslide failure. The peak velocity value of about $70\ \mathrm{m\cdot s^{-1}}$ is reached at $t = 90$ s in some parts of the SHL that have high material concentrations and sliding down steep slopes. At $t = 90$ s, the velocity averaged over the whole SHL body is ~$40\ \mathrm{m\cdot s^{-1}}$. These velocity values, peak and average, are relatively low at the initiation stage of the failure (at $t = 30$ s, in Fig. 7a) and became lower when the SHL approaches its equilibrium stage that is reached at $t = 120$ s.

3.2.2. Tsunami propagation and coastal hazard

The tsunami hazard posed by the Hirondelle SMF is evaluated by means of simulating numerically the whole source-to-coast tsunami process. This includes numerical simulations of the tsunami propagation and the maximum wave heights distribution along the coasts (pre-run-up) using 600 m-resolution gridded data. The 600 m-resolution bathymetry model is generated from two different data sets: the SWIM bathymetry compilation (Zitellini et al., 2009) and the General Bathymetric Chart of the Oceans (GEBCO) 30-arc sec gridded data (available at: http://www.gebco.net/). Fig. 8 depicts the snapshots of tsunami propagation from the source zone towards the surrounding coastal zones. The analysis of these results shows that after 5 min of propagation, tsunami waves of high amplitudes (>15 m) start travelling from the source area towards the target coasts of Iberia and north Morocco (Fig. 8a). After 40 min of tsunami propagation the waves reach the coasts in Cape S. Vicente and Madeira with amplitudes ranging from 2 to 3 m (Fig. 8b). During this propagation time, the tsunami encounters the shallow water area over the top of the Gorringe Bank, which relatively slows down the propagation and reflects a part of the incident waves (Fig. 8b). The first waves' impact along the south-western coast of Portugal, from Cape S. Vicente to Lisbon, occurred in about 1 h (Fig. 8c). The amplitude of the first incident waves along this coastal segment is about 2–3 m (Fig. 8c). Towards the African coast, the tsunami takes more time to arrive because it encounters the shallow water areas that mark the off-shore extension of the

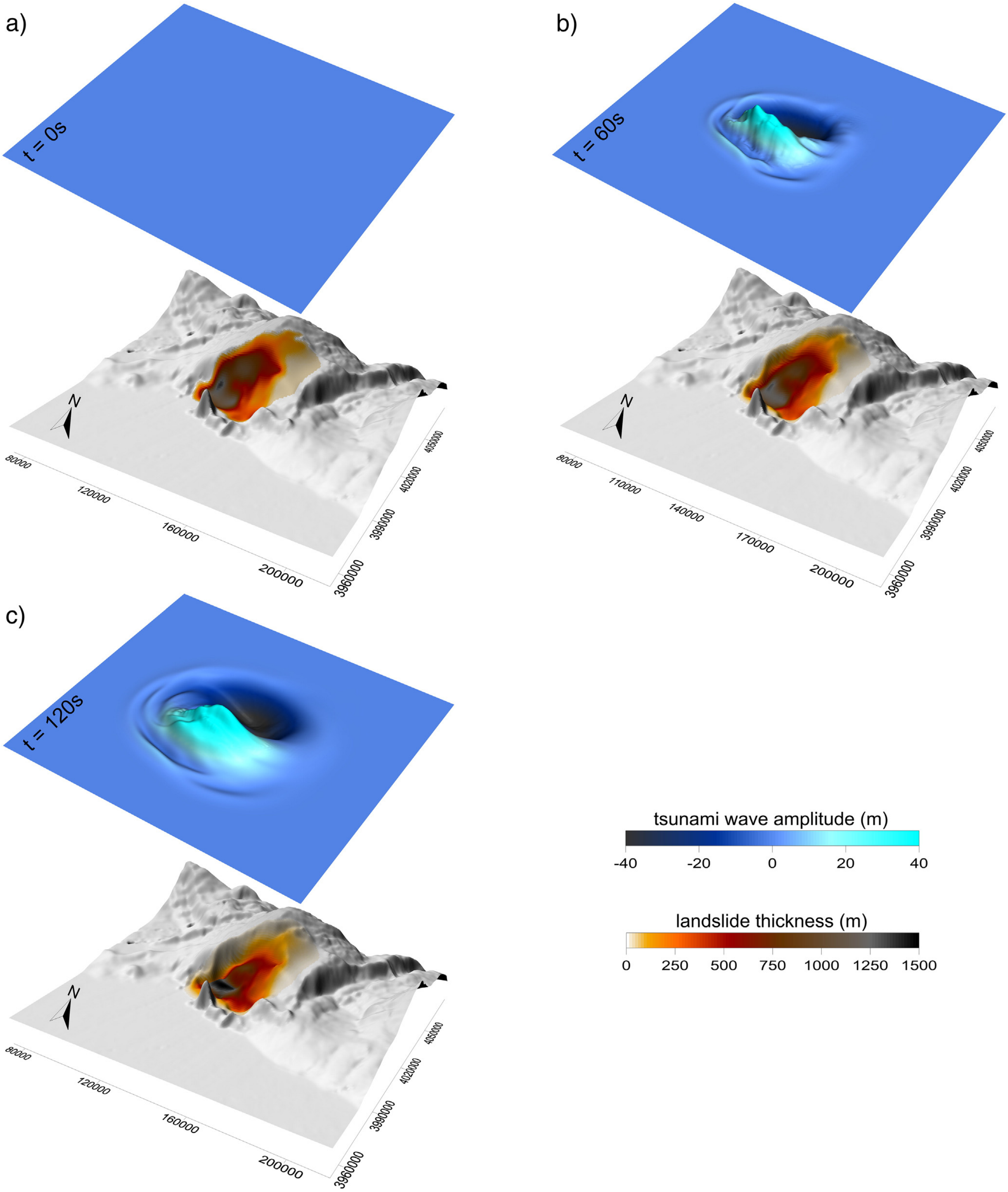

Fig. 6. Potential of tsunami generation. Snapshots of Hirondelle SMF motion (lower layer) and the subsequent tsunami generation (upper layer): a) at $t = 0$ s, the initiation of the landslide failure; b) after 60 s of the landslide failure; c) after 120 s of the landslide failure. The maps coordinates system is UTM – Zone 29 N, Datum WGS-84.

continental shelf (Fig. 8c). 95 min after the tsunami generation, the tsunami waves impact all the coasts of Portugal and Morocco, and reach the Azores Islands with amplitudes of about 3 m (Fig. 8d). The second crest generated propagates towards north with amplitude maxima of 8 m.

In Fig. 9 we present the energy patterns, in term of maximum wave amplitudes, of the tsunami caused by the failure of the South Hirondelle Landslide. The analysis of these results clearly indicates that most tsunami energy is steered towards the northern and southern sides of the Hirondelle Seamount (Fig. 9). At first order, around the generation area, the tsunami amplitude is maximal, ~40 m, in the direction of the SMF movement as well as in the opposite direction of this motion. Away from the source area, the waves undergo attenuation when

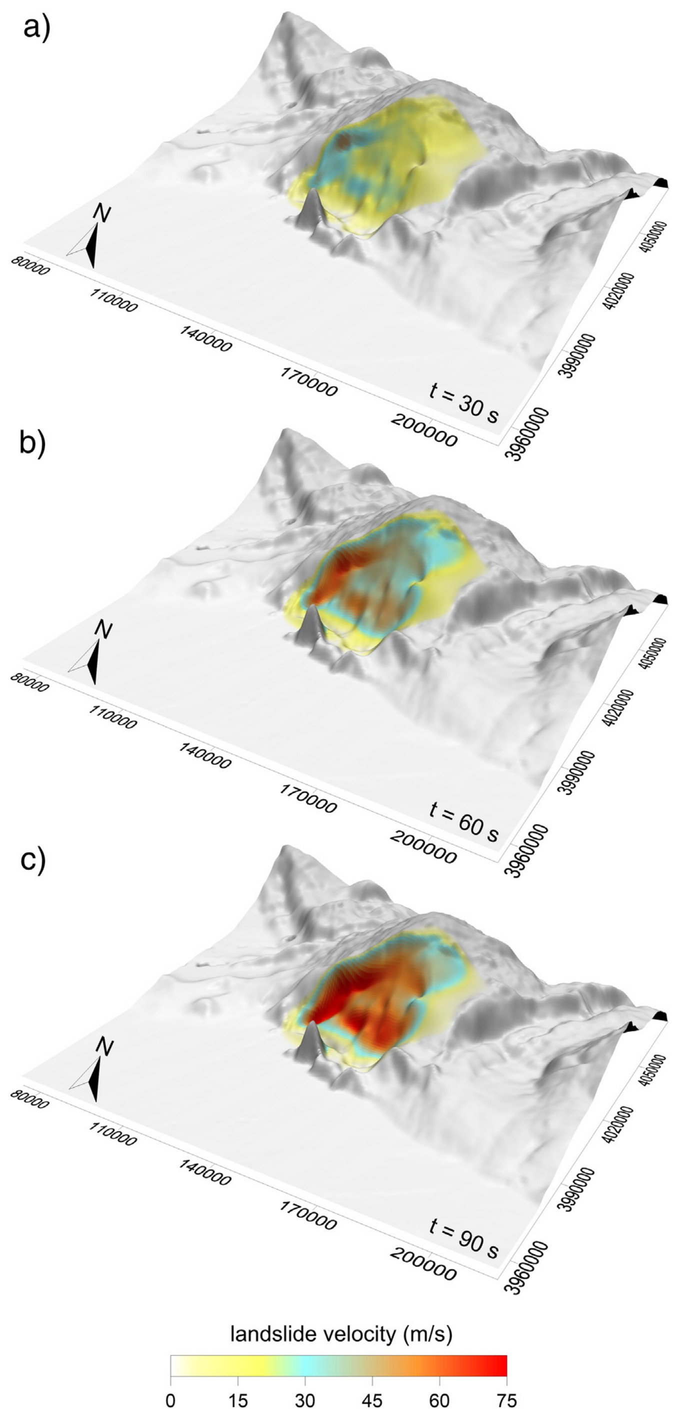

Fig. 7. Snapshots of the Hirondelle SMF velocity field: a) at $t = 30$ s after the landslide failure; b) after 60 s of the landslide failure; c) after 90 s of the landslide failure. The maps coordinates system is UTM – Zone 29 N, Datum WGS-84.

travelling towards the coasts. It is clear that the bathymetry of the region controls the maximum wave amplitudes distribution, acting, when shallow, to guide the energy towards the coast. When interacting with the coastal bathymetry the shoaling effects lead to an increase of wave height. The coastal segment north of Lisbon and along the Moroccan coast are characterized by shallow water due to the offshore extension of the continental shelf, which results in an amplification of the incident waves at those zones. Close to Lisbon the computed maximum wave amplitude reaches 14 m. Along the coast of Morocco numerical modelling predicts a maximum wave amplitude of about 15 m. The SHL-induced tsunami also reaches the Madeira, Azores and Canary Islands with wave amplitudes of 6 m, 7 m and 10 m, respectively.

4. Discussion

4.1. Landslide trigger mechanism and age of the South Hirondelle Landslide

The SHL lies within the Eurasia-Africa plate boundary zone in the Atlantic Ocean as defined by Zitellini et al. (2009), where instrumental clusters of seismicity have been recorded (Fig. 1). Instrumental earthquake events with $M_w > 7$ and epicenters within a distance of ~160 km from the SHL source area were recorded in the last decades (Buforn et al., 1988). Also one $M_w = 8.4$ event took place at ~230 km from the source of the SHL (Buforn et al., 1988). The largest historical earthquake event in western Europe, the 1st November 1755 Lisbon earthquake with estimated magnitude 8.4–8.9, with controversial seismogenic source, was also generated along this plate boundary or its close vicinity (Gutscher et al., 2002; Zitellini et al., 2009), with suggested sources that vary in distance to the SHL from ~100 km to 300 km (Terrinha et al., 2009).

Considering that the minimum water depth of the Hirondelle Seamount exceeds 2000 m and that there is no continuous morphologic connection between the SHL and the nearest continental slope and shelf, it does not seem reasonable to invoke mechanisms associated with storms or sea level variations as a probable cause for the trigger mechanism. Hence, considering that the whole sedimentary sequence is affected by the slide movement, it is here suggested that the possible source is a single earthquake event along this plate boundary or close vicinity. Although the study by ten Brink et al. (2009) refers to the geological setting and attenuation laws of the U.S. East coast, it is reported that $M_w = 7$ events generate landslides at a maximum distance of 160 km with a slope angle of 9°. The SHL displays surface slopes that can exceed 10° and the detachment slope is ~9°.

Although a seismic source is the most plausible mechanism, an aseismic source could also be envisaged due to tilting and differential sedimentary load. An alternative aseismic source could be instability caused by building-up of the continuous tectonic deformation of the sedimentary package caused by the propagation of faults at the corner zone formed by the Gorringe thrust and the Hirondelle Seamount. It was shown by Rosas et al. (2012) that faults connecting strike-slip faults and thrusts form on the foot-wall of the thrust and become parallel to the strike-slip faults as they approach them (Fig. 2). The case study used by Rosas et al. (2012) was based on numerical and physical modelling of a natural analogue of the intersection of the Horseshoe fault and SWIM faults in the close vicinity of the Hirondelle Seamount. Alternatively, it is a possibility that the mantle rooted blind faults connecting the Gorringe thrust and the Hirondelle Seamount may account for the observed seismicity (Figs. 1 and 2).

An accurate age of the SHL should be based on the study of seafloor sediments, which has not been done. However, because the post-Lower Miocene seismo-stratigraphy does not show unconformities within UIV it seems that the Quaternary record is continuous, probably made up of hemipelagic sedimentation. Since the whole stratigraphic package is deformed by the landslide movement a Quaternary age is suggested, possibly a Late Pleistocene age as reported for other events by Gràcia et al. (2010) and Lo Iacono et al. (2012) for the Marquês de Pombal landslides and for the North Gorringe Landslide shown in Fig. 2.

4.2. Tsunamigenic potential of the South Hirondelle Landslide and propagation patterns

The generation of a tsunami from a submarine landslide is, in general, controlled by intrinsic characteristics, such as the volume, the type and density of the material, the lithologic composition, the thickness, the kinematic viscosity (Chaytor et al., 2009; Geist et al., 2009), and

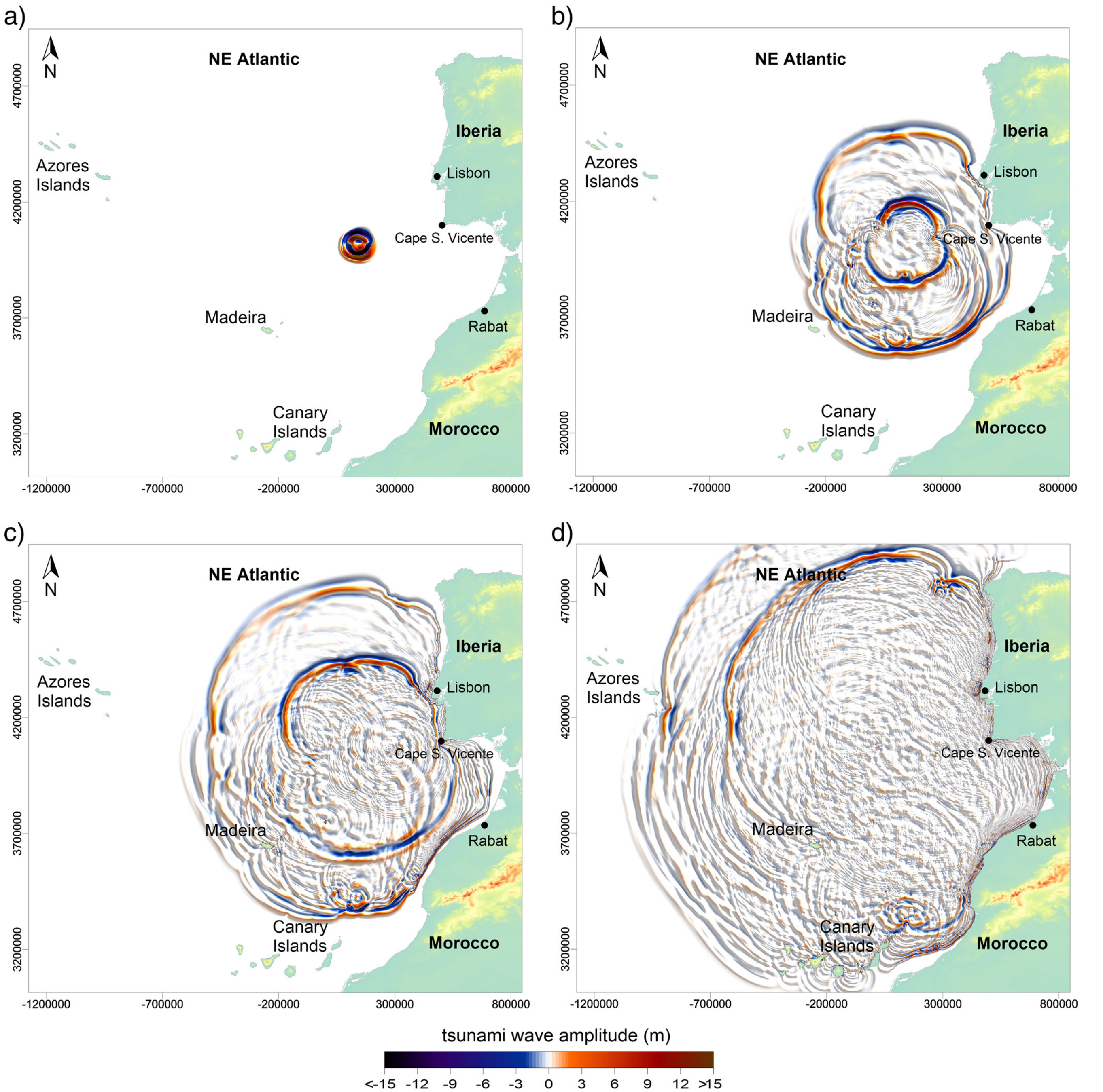

Fig. 8. Tsunami waves propagation in the NE Atlantic region following the failure of the Hirondelle submarine landslide. The propagation snapshots are plotted after: a) 5 min of propagation; b) 45 min of propagation; c) 60 min of propagation; d) 95 min of propagation. The maps coordinates system is UTM – Zone 29 N, Datum WGS-84.

the environmental constraints in which the failure occurs, such as the water depth and the slope gradient (Pelinovsky and Poplavsky, 1996). Even though deep-water submarine landslides have less potential in generating strong tsunami waves (Masson et al., 2006; Harbitz et al., 2006), we have shown through numerical simulations that the SHL, located at a depth between approximately 2.5 and 4.7 km, may have generated a large tsunami. This is mainly due to the fact that the failure of SHL involves a volume of hundred cubic kilometres of sediments (~500 km^3) with large thickness (max of ~1500 m) that starts sliding over a relatively steep slope (between 10° and 3.5°, see Fig. 2b, and reaching 16°). All these factors led to a fast failure of the SHL, average velocity over the whole landslide body reached ~40 $m \cdot s^{-1}$ at 90 s after the failure, resulting in a significant vertical displacement of the sea-floor and therefore in a generation of a large tsunami.

The tsunami hazard is addressed here through the worst-case scenario assuming a unique failure of the SHL. Although it is likely that the SHL corresponds to a single event, we cannot exclude the possibility of a sequence of small failures emplaced over a short period. To account for this possibility, we simulate the SHL-induced tsunami considering two additional SMF scenarios: i) the failure of a half of the volume considered for the SHL, and ii) a sequence of two failures, half of SHL volume each, with a time lag of 2.5 min. Results of tsunami modelling for these two scenarios are depicted in Figs. 10 and 11. The failure of the half of the volume considered for the SHL would generate a tsunami wave up to 20 m in amplitude (Fig. 10a) that hit the SW Iberian and Moroccan coasts with wave reaching 6 m (Fig. 10b). Simulations of the tsunami caused by the failure of SHL in a sequence of two SMFs indicate the generation of two successive waves with a maximum amplitude up to 25 m

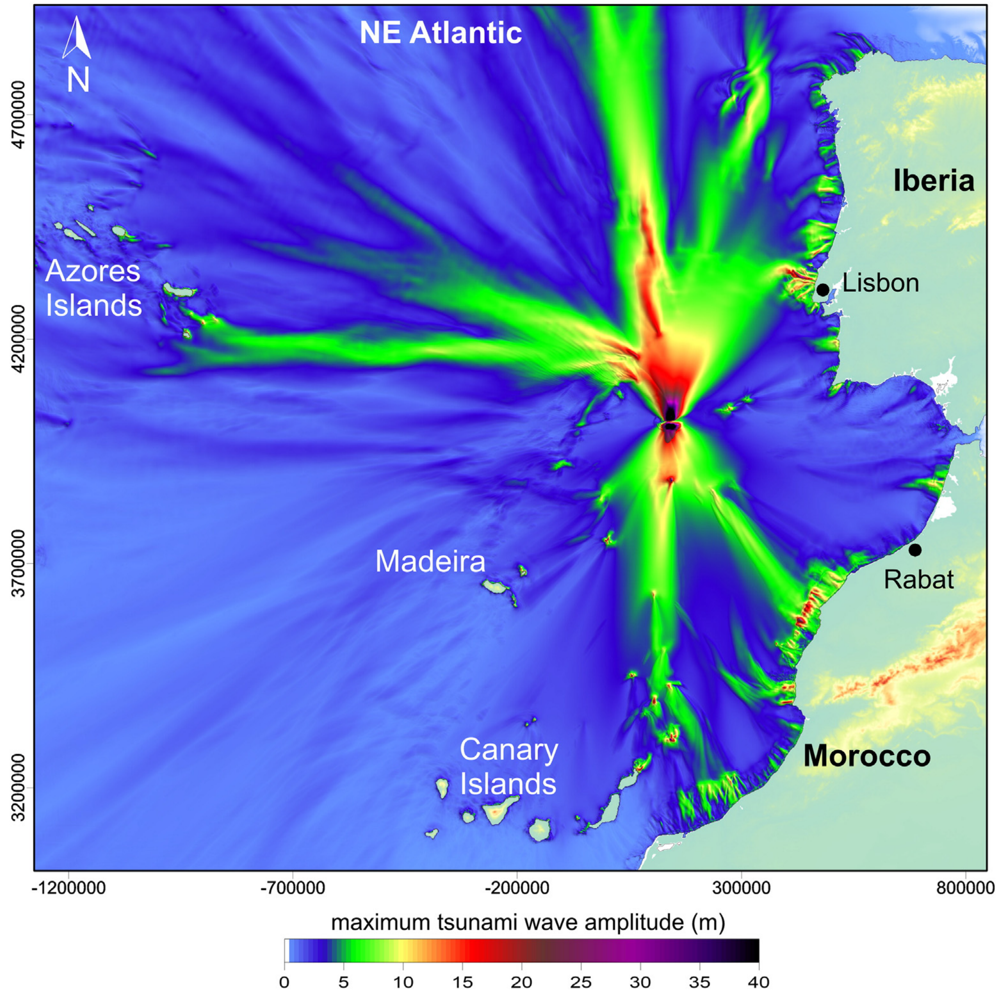

Fig. 9. Tsunami maximum wave amplitudes distribution in the NE Atlantic region due to the occurrence of the South Hirondelle submarine landslide. The map coordinates system is UTM – Zone 29 N, Datum WGS-84.

(Fig. 11a). The overall effect of the tsunami impact from this scenario (Fig. 11b) shows that the NE Atlantic coasts may experience waves up to 7 m at some locations. Therefore, smaller landslide volumes still present a significant threat for the SW Iberian and Moroccan coasts, and cannot be neglected in coastal geo-hazard assessment for the NE Atlantic region.

The Hirondelle Seamount is surrounded by a number of oceanic features, namely the Gorringe Bank to the east, the Coral Patch Ridge to the south and the Madeira-Tore Rise to the west (Fig. 1a for location). All these bathymetric structures affect the SHL-induced tsunami propagation. The presence of the Gorringe Bank at the eastern side of the SHL slows down the tsunami propagation and reflects a part of the incident waves, which can result in a loss of tsunami energy steered towards the south-western coasts of Iberia. Towards the south, the tsunami waves encounter the Coral Patch Ridge that leads to significant reflections of the waves. This ridge appears to play the role of a barrier that partially protects the southern Moroccan coast. At the west of the SHL, the Madeira-Tore Rise also seems to play the same role in protecting the coasts of the Madeira Islands.

The tsunami caused by the SHL seems to have a regional impact as the waves travelled with relatively large amplitudes from the source area towards various coastal zones of the NE Atlantic. Despite the fact that the tsunamis caused by the submarine landslides undergo a significant attenuation of the waves when travelling far-away from the source area (Okal and Synolakis, 2004; Harbitz et al., 2006), as it is the case of the SHL, an important tsunami energy remains steered particularly towards the north. Also, when the tsunami reaches the shallow water areas, it encounters the continental shelf extended along various coastal zones, which lead to an important amplification of the incident waves. These shoaling effects occur in particular north of Lisbon-Portugal and along the coast of Morocco. Another effect is due to the shallow water areas along the Gloria Fault that channel the wave energy towards the Azores Islands.

In the NE Atlantic only few studies addressed the landslide-induced tsunami hazard on the coasts of Iberia and Morocco. Lo Iacono et al. (2012) investigated the Gorringe Bank deep-water landslide and showed that it may cause a major tsunami waves reaching the coasts of Portugal. The Gorringe Bank landslide has an estimated volume of ~80 km^3 that is distributed between the depths of 2900 m and 5100 m. The numerical simulations predict an initial wave of ~20 m and an impact along the Portuguese coasts with waves reaching 7 to 20 m after 30 min of propagation. On the other hand, our case of SHL has similar depth but different volume and source characteristics when compared to the Gorringe Bank landslide. These differences result in the generation of a bigger tsunami that takes more time (~45 min) to reach the coast of Portugal. Even though both events present different characteristics, the GB landslide is a rock fall involving different tsunami generation mechanism, we find a similarity in the wave energy distribution, in particular in the near-shore mainly due to the morphologic configuration of the area.

It is important to mention here that this study suffers from some limitations regarding the models considered. The main simplification concerns the rheological model adopted to represent the landslide material and its dynamics, which mainly affects the tsunami generation.

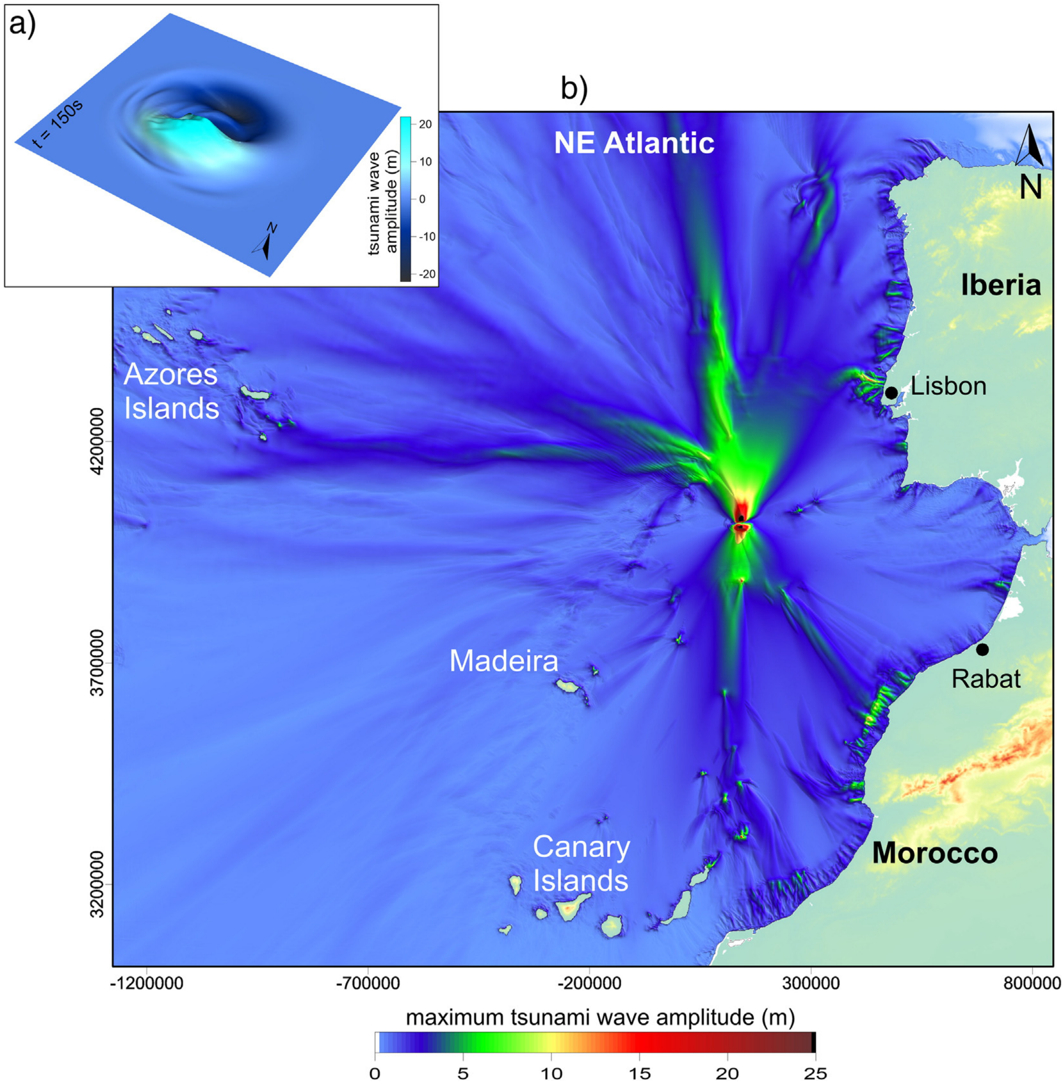

Fig. 10. Tsunami simulation results due to the occurrence of a smaller landslide, half of the volume considered for the South Hirondelle Landslide: a) Tsunami generation; and b) Tsunami maximum wave amplitudes distribution in the NE Atlantic region. The map coordinates system is UTM – Zone 29 N, Datum WGS-84.

A better representation of the landslide rheological model requires geotechnical analyses of sediment cores, which are extremely expensive to collect and are seldom available. Also, the reconstruction of the pre-event landslide was based on the interpretation of only one multichannel profile in addition to the scar observed in the bathymetry. Despite these limitations, this study is an important contribution to assess the landslide generated tsunami hazard in the NE Atlantic region.

In addition to the Hsm and GB, the NE Atlantic region in the Eurasia-Africa plate boundary area comprehends a number of seamounts (e.g., the Josephine, the Marquês de Pombal, and the Coral Patch). These oceanic features have similar vigorous morphology, with average slopes dipping ~3.8° to 4.7° that strongly contrasts with the surrounding abyssal plains that have slopes of <0.1°. Within these seamounts, it is well known that many of the triggered landslides occurred in Late Pleistocene and Holocene times (Gràcia et al., 2010). The pre-conditioning and triggering mechanisms of SMFs, mainly consisting of moderate to high magnitude seismicity and tectonic driven gravity instability, still persist in the region, and therefore, favor the triggering of future large SMFs. This study and the study by Lo Iacono et al. (2012) clearly show the significant tsunamigenic potential of such SMFs occurring in deep-water seamounts. Both studied features, Hsm and GB landslides, can form a starting point to construct a reliable deep-water tsunamigenic SMFs database for the region. This database must be completed with more quantitative information on the rheological properties and chronology of the existent SMFs for a comprehensive geo-hazard assessment in the region. Moreover, slope stability analysis for the main deep-water seamounts in the region requires more attention in order to mitigate future failures as well as their possible tsunamigenic potential.

5. Conclusions

In this paper we investigated the possible tsunami and its coastal impact caused by a deep water submarine mass failure in the NE Atlantic. The Hirondelle Seamount case study, located at water depths >2000 m, has a large mass transported deposit. The main findings of this work are:

i. The occurrence of a large submarine landslide (SHL) involving a volume 500 km^3 of sediments deposit and the mapping of its corresponding scar and source area.
ii. The SHL occurred as one single landslide event as sustained from inspection of multichannel reflection seismic profile.
iii. The SHL caused a significant tsunami despite being located in a deep-water region.
iv. The SHL had a regional impact along the surrounding coasts of the NE Atlantic region, in particular along the coasts of Morocco and Iberia.

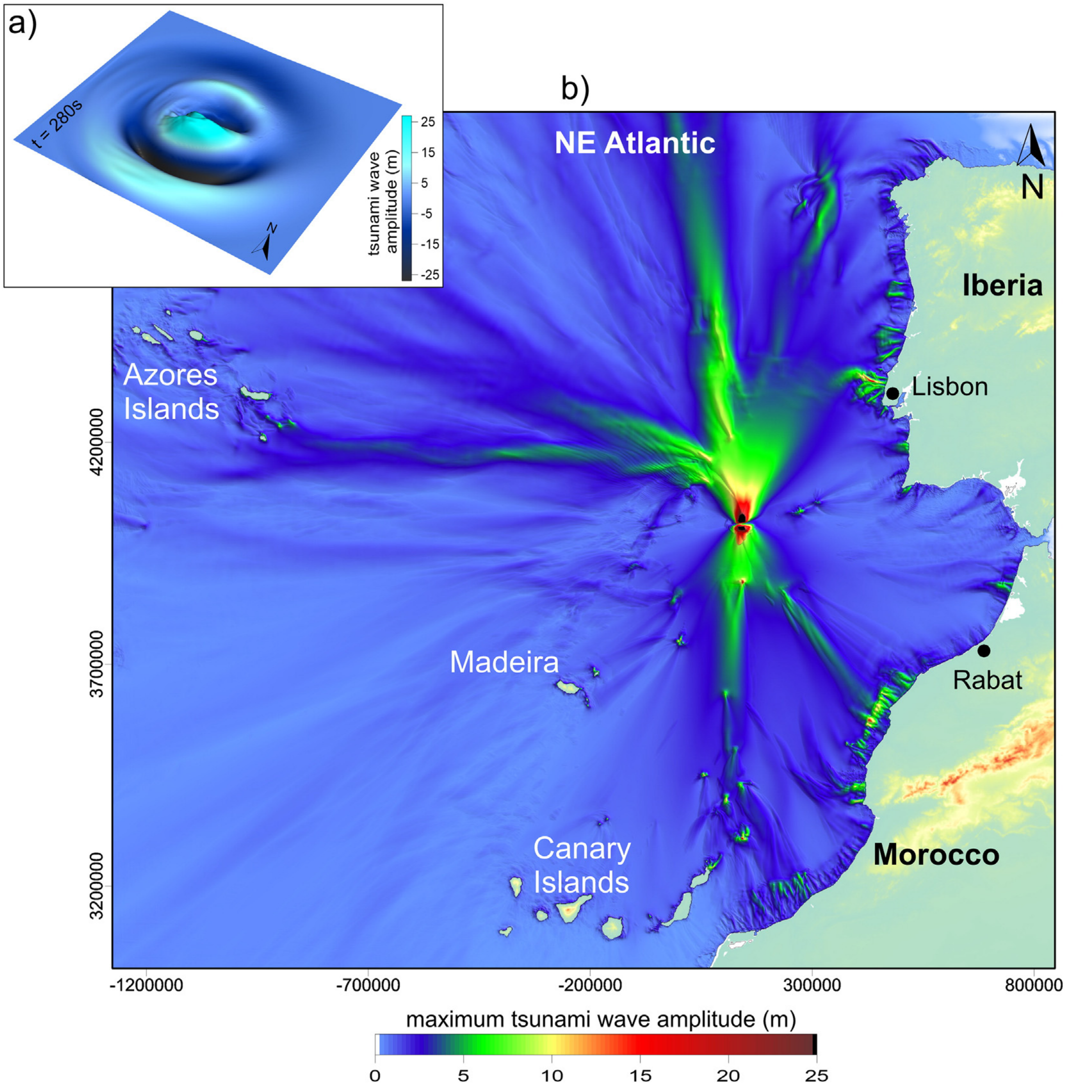

Fig. 11. Tsunami simulation results due to the occurrence of the South Hirondelle Landslide as a sequence of two landslides emplaced over 2.5 min period: a) Tsunami generation; and b) Tsunami maximum wave amplitudes distribution in the NE Atlantic region. The map coordinates system is UTM – Zone 29 N, Datum WGS-84.

v. The SHL-induced tsunami took tens of minutes (45–60 min) to reach the Portuguese and Moroccan coasts.

In summary, this paper presents a contribution to the study of the tsunami hazard associated to non-seismic sources in the NE Atlantic. In addition, it is suggested that in the NE Atlantic more attention should be given to tsunami hazard assessment due to the landslides occurring in the deep-water seamounts.

Acknowledgements

This work is funded by the EU project ASTARTE - Assessment, Strategy And Risk Reduction for Tsunamis in Europe, Grant 603839, 7th FP (ENV.2013.6.4-3) and by the Portuguese Foundation for Science and Technology – FCT project CONDRIBER, Grant PTDC/GEO-GEO/4430/2012. The support by Landmark Graphics Corporation via the Landmark University Grant Program is also acknowledged. The authors would like to thank the Editor M. Rebesco, C. Lo Iacono and an anonymous reviewer for their timely and helpful reviews, which improved the manuscript.

References

Assier-Rzadkiewicz, S.A., Mariotti, C., Heinrich, P., 1997. Numerical simulation of submarine landslides and their hydraulic effects. J. Waterw. Port Coast. Ocean Eng. 123 (4), 149–157.
Auzende, J.M., Charvet, J., Le Lann, A., Le Pichon, X., Monteiro, J.H., Nicolas, A., Olivet, J.L., Ribeiro, A., 1978. Le Banc de Gorringe: résultats de la campagne CYAGOR (août 1977). Bull. Soc. Géol. 545–556 (7 serie, t. XXI, n 5).
Bondevik, S., Løvholt, F., Harbitz, C., Mangerud, J., Dawson, A., Inge Svendsen, J., 2005. The Storegga Slide tsunami-comparing field observations with numerical simulations. Mar. Pet. Geol. 22 (1), 195–208.
Bird, P., Kagan, Y.Y., 2004. Plate-tectonic analysis of shallow seismicity: apparent boundary width, Beta, corner magnitude, coupled lithosphere thickness, and coupling in seven tectonic settings. Bull. Seismol. Soc. Am. 94 (6), 2380–2399.
Buforn, E., Udías, A., Colombás, M.A., 1988. Seismicity, source mechanisms and tectonics of the Azores-Gibraltar plate boundary. Tectonophysics 152 (1–2), 89–118.
Chaytor, J.D., Uri, S., Solow, A.R., Andrews, B.D., 2009. Size distribution of submarine landslides along the US Atlantic margin. Mar. Geol. 264 (1), 16–27.
Clague, J.J., 2001. Tsunamis. A Synthesis of Geological Hazards in Canada. Vol. 548, pp. 27–42.
De Alteriis, G., Passaro, S., Tonielli, R., 2003. New, high resolution swath bathymetry of Gettysburg and Ormonde Seamounts (Gorringe Bank, eastern Atlantic) and first geological results. Mar. Geophys. Res. 24 (3–4), 223–244.
Fine, I.V., Rabinovich, A.B., Bornhold, B.D., Thomson, R.E., Kulikov, E.A., 2005. The Grand Banks landslide-generated tsunami of November 18, 1929: preliminary analysis and numerical modeling. Mar. Geol. 45–57 (215 (1-2 SPEC ISS).
Fine, I.V., Rabinovich, A.B., Thomson, R.E., Kulikov, E.A., 2003. Numerical Modeling of Tsunami Generation by Submarine and Subaerial Landslides. In: Yalciner, A.C.,

Pelinovsky, E.N., Synolakis, C.E., Okal, E. (Eds.), Submarine Landslides and TsunamisNATO Advanced Series. Kluwer Academic Publication, Dordrecht, pp. 69–88.

Geissler, W.H., Matias, L., Stich, D., Carrilho, F., Jokat, W., Monna, S., IbenBrahim, A., Mancilla, F., Gutscher, M.-A., Sallarès, V., Zitellini, N., 2010. Focal mechanisms for sub-crustal earthquakes in the Gulf of Cadiz from a dense OBS deployment. Geophys. Res. Lett. 37 (18).

Geist, E.L., Lynett, P.J., Chaytor, J.D., 2009. Hydrodynamic modeling of tsunamis from the Currituck landslide. Mar. Geol. 264 (1), 41–52.

Girardeau, J., Cornen, G., Agrinier, P., Beslier, M.-O., Dubuisson, G., Le Gall, B., Monnier, C., Pinheiro, L., Ribeiro, A., Whitechurch, H., 1998. Preliminary results of Nautile dives on the Gorringe Bank (West Portugal). Comp. Rend. Acad. Scie. Ser. IIA Earth Planet. Scie. 4 (326), 247–254.

Gràcia, E., Vizcaino, A., Escutia, C., Asioli, A., Rodes, A., Pallas, R., Garcia-Orellana, J., Lebreiro, S., Goldfinger, C., 2010. Holocene earthquake record offshore Portugal (SW Iberia): testing turbidite paleoseismology in a slow-convergence margin. Quat. Sci. Rev. 29 (9), 1156–1172.

Gràcia, E., Danobeitia, J., Vergés, J., Bartolomé, R., Córdoba, D., 2003. Crustal architecture and tectonic evolution of the Gulf of Cadiz (SW Iberian margin) at the convergence of the Eurasian and African plates. Tectonics 22 (4).

Gutscher, M.A., Malod, J., Rehault, J.P., Contrucci, I., Klingelhoefer, F., Mendes-Victor, L., Spakman, W., 2002. Evidence for active subduction beneath Gibraltar. Geology 30 (12), 1071–1074.

Harbitz, C.B., Lovholt, F., Pedersen, G., Masson, D.G., 2006. Mechanisms of tsunami generation by submarine landslides: a short review. Nor. J. Geol. 86, 255–264.

Harbitz, C.B., 1992. Model simulations of tsunamis generated by the Storegga slides. Mar. Geol. 105, 1–21.

Hayes, D.E., Pimm, A.C., Beckmann, J.P., Benson, W.E., Berger, W.H., Roth, P.H., Supko, P.R., von Rad, U., 1972. Initial Reports of the Deep Sea Drilling Project, Site DSDP. p. 135 http://dx.doi.org/10.2973/dsdp.proc.14.102.1972.

Hayward, N., Watts, A.B., Westbrook, G.K., Collier, J.S., 1999. A seismic reflection and GLORIA study of compressional deformation in the Gorringe Bank Region, Eastern North Atlantic. Geophys. J. Int. 138, 831–850.

Heinrich, P., Piatensai, A., Okal, E., Hebert, H., 2000. Near-field modelling of the July 17, 1998 tsunami in Papua New Guinea. Geophys. Res. Lett. 27, 3037–3040 (2.3.4).

Hernández-Molina, F.J., Llave, E., Preu, B., Ercilla, G., Fontan, A., Bruno, M., Serra, N., Gomiz, J.J., Brachenridge, R.E., Sierro, F.J., Stow, D.A.V., García, M., Juan, C., Sandoval, N., Arnaiz, A., 2014. Contourite processes associated with the Mediterranean outflow water after its exit from the Strait of Gibraltar: global and conceptual implications. Geology 42 (3), 227–230.

Imamura, F., Hashi, K., Imteaz, M., 2001. Modeling for Tsunamis Generated by Landsliding and Debris Flow. Tsunami Research at the End of a Critical Decade. Springer Netherlands, pp. 243–282.

Jiang, L., LeBlond, P.H., 1994. Three-dimensional modeling of tsunami generation due to a submarine mudslide. J. Phys. Oceanogr. 24 (3), 559–572.

Jiménez-Munt, I., Fernàndez, M., Vergés, J., Afonso, J.C., Garcia-Castellanos, D., Fullea, J., 2010. Lithospheric structure of the Gorringe Bank: insights into its origin and tectonic evolution. Tectonics 29 (5), TC5019. http://dx.doi.org/10.1029/2009TC002458.

Kawata, Y., Benson, B.C., Borrero, J.L., Davies, H.L., de Lange, W.P., Imamura, F., Nott, J., Synolakis, C.E., 1999. Tsunami in Papua New Guinea was as intense as first thought. Eos 80 (101), 102–103.

Lo Iacono, C., Gràcia, E., Zaniboni, F., Pagnoni, G., Tinti, S., Bartolomé, R., Masson, D.G., Russell, B.W., Lourenço, N., Abreu, M.P., Dañobeitia, J.J., Zitellini, N., 2012. Large, deep water slope failures: implications for landslide-generated tsunamis. Geology 40 (10), 931–934.

Martinez-Loriente, S., Gràcia, E., Bartolome, R., Sallarès, V., Connors, C., Perea, H., Iacono, L., Klaeschen, D., Terrinha, P., Dañobeitia, J.J., Zitellini, N., 2013. Active deformation in old oceanic lithosphere and significance for earthquake hazard: seismic imaging of the Coral Patch Ridge area and neighboring abyssal plains (SW Iberian Margin). Geochem. Geophys. Geosyst. 14 (7), 2206–2231. http://dx.doi.org/10.1002/ggge.20173.

Masson, D.G., Harbitz, C.B., Wynn, R.B., Pedersen, G., Løvholt, F., 2006. Submarine landslides: processes, triggers and hazard prediction. Phil. Trans. R. Soc. A 364 (1845), 2009–2039.

McSaveney, M.J., Goff, J.R., Darby, D.J., Goldsmith, P., Barnett, A., Elliott, S., Nongkas, M., 2000. The 17 July 1998 tsunami, Papua New Guinea: evidence and initial interpretation. Mar. Geol. 170 (1), 81–92.

Medialdea, T., Vegas, R., Somoza, L., Vazquez, J.T., Maldonado, A., Diaz-del Rio, V., Maestro, A., Cordoba, D., Fernandes-Puga, M.C., 2004. Structure and evolution of the "Olistostrome" complex of the Gibraltar Arc in the Gulf of Cádiz (eastern Central Atlantic): evidence from two long seismic cross-sections. Mar. Geol. 209 (1), 173–198.

Murty, T.S., 1977. Seismic sea waves: tsunamis (No. 198). Department of Fisheries and the Environment. Fish. Mar. Ser.

Okal, E.A., Synolakis, C.E., 2004. Source discriminants for near-field tsunamis. Geophys. J. Int. 158 (3), 899–912.

Pelinovsky, E., Poplavsky, A., 1996. Simplified model of tsunami generation by submarine landslides. Phys. Chem. Earth 21 (1), 13–17.

Rabinovich, A.B., Thomson, R.E., Bornhold, B.D., Fine, I.V., Kulikov, E.A., 2003. Numerical modelling of tsunamis generated by hypothetical landslides in the Strait of Georgia, British Columbia. Pure Appl. Geophys. 160 (7), 1273–1313.

Roque, C., Duarte, H., Terrinha, P., Valadares, V., Noiva, J., Cachão, M., Ferreira, J., Legoinha, P., Zitellini, N., 2012. Pliocene and Quaternary depositional model of the Algarve margin contourite drifts (Gulf of Cadiz, SW Iberia): seismic architecture, tectonic control and paleoceanographic insights. Mar. Geol. 303, 42–62.

Roque, C., 2007. Tectonostratigrafia Do Cenozóico Das Margens Continentais Sul e Sudoeste Portuguesas: Um Modelo de correlação sismostratigráfica (PhD thesis) Department of Geology, University of Lisbon (in Portuguese, 310 pp.).

Rosas, F.M., Duarte, J.C., Neves, M.C., Terrinha, P., Silva, S., Matias, L., Gràcia, E., Bartolomé, R., 2012. Thrust–wrench interference between major active faults in the Gulf of Cadiz (Africa–Eurasia plate boundary, offshore SW Iberia): tectonic implications from coupled analog and numerical modeling. Tectonophysics 548, 1–21.

Ryan, W.B.F., Hsü, K.J., Cita, P.D., M.B., Lort, J., Maync, W., Nesteroff, W.D., Pautot, G., Stradner, H., Wezel, F.C., 1973. Site DSDP 120. Initial Rep. Deep Sea Drill. Proj. http://dx.doi.org/10.2973/dsdp.proc.13.102.1973.

Sallarès, V., Martínez-Loriente, S., Prada, M., Gràcia, E., Ranero, C.R., Gutscher, M.A., Bartolome, R., Gailler, A., Dañobeitia, J.J., Zitellini, N., 2013. Seismic evidence of exhumed mantle rock basement at the Gorringe Bank and the adjacent horseshoe and Tagus abyssal plains (SW Iberia). Earth Planet. Sci. Lett. 365, 120–131. http://dx.doi.org/10.1016/j.epsl.2013.01.021.

Sartori, R., Torelli, L., Zitellini, N., Peis, D., Lodolo, E., 1994. Eastern segment of the Azores–Gibraltar line (central–eastern Atlantic): an oceanic plate boundary with diffuse compressional deformation. Geology 22, 555–558.

Schmincke, H.-U., Weaver, P.P.E., Firth, J.V., 1995. Background, Objectives, and Principal Results of Drilling the Clastic Apron of Gran Canaria (VICAP). In: Schmincke, H.-U., Weaver, P.P.E., Firth, J.V. (Eds.), Proc. ODP, Init. Repts. Vol. 157. Ocean Drilling Program, College Station, TX, pp. 11–25. http://dx.doi.org/10.2973/odp.proc.ir.157.1995

Seton, M., Müller, R.D., Zahirovic, S., Gaina, C., Torsvik, T., Shephard, G., Talsma, A., Gurnis, M., Turner, M., Maus, S., Chandler, M., 2012. Global continental and ocean basin reconstructions since 200 Ma. Earth Sci. Rev. 113 (3–4), 212–270.

Synolakis, C.E., Bardet, J.P., Borrero, J.C., Davies, H.L., Okal, E.A., Silver, E.A., Sweet, S., Tappin, D.R., 2002. The slump origin of the 1998 Papua New Guinea tsunami. Proc. R. Soc. Lond. A 458, 763–789.

Tappin, D.R., Watts, P., McMurty, G.M., Lafoy, Y., Matsumoto, T., 2001. The Sissano, Papua New Guinea tsunami of July 1998—offshore evidence on the source mechanism. Mar. Geol. 175, 1–24. http://dx.doi.org/10.1016/S0025-3227(01)00131-1.

ten Brink, U.S., Lee, H.J., Geist, E.L., Twichell, D., 2009. Assessment of tsunami hazard to the U.S. East Coast using relationships between submarine landslides and earthquakes. Mar. Geol. 264 (1), 65–73.

Terrinha, P., Matias, L., Vicente, J., Duarte, J., Luis, J., Pinheiro, L., Lourenço, N., Diez, S., Rosas, Magalhães, V., Valadares, V., Zitellini, N., Roque, C., MATESPRO Team, 2009. Morphotectonics and strain partitioning at the Iberia–Africa plate boundary from multibeam and seismic reflection data. Mar. Geol. 267 (3), 156–174.

Terrinha, P., Pinheiro, L.M., Henriet, J.-P., Matias, L., Ivanov, M.K., Monteiro, J.H., Akhmetzhanov, A., Volkonskaya, A., Cunha, T., Shaskin, P., Rovere, M., The TTR10 Shipboard Scientific Party, 2003. Tsunamigenic-seismogenic structures, neotectonics, sedimentary processes and slope instability on the southwest Portuguese Margin. Mar. Geol. 195 (1), 55–73. http://dx.doi.org/10.1016/S0025-3227(02)00682-5.

Thomson, R.E., Rabinovich, A.B., Kulikov, E.A., Fine, I.V., Bornhold, B.D., 2001. On Numerical Simulation of the Landslide-Generated Tsunami of November 3, 1994 in Skagway Harbor, Alaska. Tsunami Research at the End of a Critical Decade. Springer Netherlands, pp. 243–282.

Torelli, L., Sartori, R., Zitellini, N., 1997. The giant chaotic body in the Atlantic Ocean off Gibraltar: new results from a deep seismic reflection survey. Mar. Pet. Geol. 14 (2), 125–138.

Zitellini, N., Gràcia, E., Matias, L., Terrinha, P., Abreu, M.A., DeAlteriis, G., Heriet, J.P., Dañobeitia, J.J., Masson, D.G., Mulderi, T., Ramella, R., Somoza, L., Diez, S., 2009. The quest for the Africa–Eurasia plate boundary west of the Strait of Gibraltar. Earth Planet. Sci. Lett. 280 (1), 13–50.

Zitellini, N., Rovere, M., Terrinha, P., Chierici, F., Matias, L., Team, B., 2004. Neogene through Quaternary tectonic reactivation of SW Iberian passive margin. Pure Appl. Geophys. 161 (3), 565–587.